Active Seismic Refraction, Reflection and Surface-Wave Surveys in Thick Debris-Covered Glacial Environments

Tyler Kuehn[1], John W. Holt[1,2], Roy Johnson[1], Tyler Meng[2]

[1]University of Arizona Department of Geosciences

[2]University of Arizona Lunar and Planetary Laboratory

Corresponding author: Tyler Kuehn (tkuehn@arizona.edu)

Key Points:

- We use ultra-dense receiver spacing to image seismic reflections from the loose debris layer on a debris-covered glacier for the first time.
- We demonstrate we can obtain shear-wave velocity structure (stiffness) observations for debris cover on glaciers.

Abstract

Debris-covered glaciers and rock glaciers have been increasingly studied in recent years because of the role they play within local watersheds, glacial ablation models due to climate change, and as analogs for buried ice features on planetary bodies such as Mars. Characterizing the supraglacial debris layer is a large part of these efforts. Geophysical exploration of debris-covered glaciers has mostly excluded active seismic methods, with the exception of refraction studies, due to the attenuating properties of the debris cover and field survey efficiency. We evaluate the accuracy, field efficiency, and effectiveness of seismic refraction, reflection, and surface-wave surveys for determining the elastic properties of the debris layer and any underlying layers on debris-covered glaciers using sites from Sourdough Rock Glacier and in the Malaspina Glacier forelands in Southcentral Alaska. We compare our seismic results with our results from ground-penetrating radar. Our results indicate that the interface between the debris layer and the ice can be imaged using seismic reflection methods, and that multi-channel analysis of surface waves (MASW) can provide insight to the variability of the shear-wave structure within the debris layer. We image an ultra-shallow seismic reflection from the bottom of the loose debris layer using ultra-dense receiver arrays. This study also presents results using multi-channel analysis of surface waves (MASW) on a debris-covered glacier, which we find could be a valuable addition to the toolbox of future geophysical investigations on these landforms.

Plain Language Summary

Debris-covered glaciers and rock glaciers are glaciers with a loose rock layer covering all or most of their surface. This layer can be several meters thick and plays an important role in how fast the glacier melts. These types of glaciers are an important analog to similar buried ice features we observe on other planetary bodies, such as Mars. Typically, the subsurface of these glaciers is studied using the geophysical method of ground-penetrating radar, though in this paper we explore how active-source seismic methods could be utilized in future surveys. We demonstrate that using active-seismic techniques can provide information on the 'stiffness' of the debris layer, which can add context to a ground-penetrating radar survey and ultimately aid in interpreting glacial features.

1 Introduction1.1 Background and Motivation

Debris-covered glaciers (DCG) are unique geomorphological landforms that can be found across the globe anywhere clean-surfaced glaciers are formed, in high mountain environments where there is an abundant supply of rockfall debris. They are characterized by a surficial debris cover that varies in thickness spanning the accumulation zone to the glacier terminus. The debris layer acts as insulation for the subsurface ice, decreasing the ablation rate with increasing debris thickness (Östrem, 1959; see also Nicholson & Benn, 2006). The factors that contribute to the evolution of the debris surface and the physical properties within the debris are being increasingly studied in recent years to better understand the response of DCG to climate change (Rowan et al., 2015; Scherler et al., 2011; Yde & Paasche, 2010) and the effects on local watersheds, glacial hazards and landscape evolution.

In addition to these terrestrial applications, DCG have important planetary exploration implications for similar features observed on Mars (Head et al., 2010; Holt et al., 2008; Levy et al., 2014). Using DCG on Mars as a potential water resource for future exploration efforts and human habitation missions has been a recent topic in the planetary exploration community (Abbud-Madrid et al., 2016). Thickness of the debris layer, clast size distribution, and presence of ice-cemented debris are important parameters affecting the feasibility of in-situ resource utilization that need to be accurately constrained in future planetary exploration studies.

Remote alpine environments and rugged terrain make exploration of debris-covered glaciers on Earth by drilling methods prohibitive in both cost and logistics to be widely used. For that reason, studies of the debris layer and internal structure of DCG have mostly relied on remote sensing data and geophysical exploration (Bhardwaj et al., 2014; Merz et al., 2016; Paul et al., 2004). Among the suite of geophysical tools to study DCG, ground-penetrating radar (GPR) has been the most widely employed method for debris layer thickness investigations (e.g. Florentine et al., 2014; Petersen et al., 2020), because of the ease of use in rugged field settings and capability of imaging subsurface glacial structure. In contrast, active seismic exploration methods have not been widely used on DCG with thick debris cover largely because of field efficiency issues and signal-to-noise ratios affected by the highly attenuating debris layer. Active-source seismic studies have been limited to (*p*)-wave refraction profiles and seismic refraction tomography (SRT), which have been shown to accurately delineate zones of pure ice from debris in ice-cored moraines and debris-covered glaciers (Croce & Milana, 2002; Langston et al., 2011; Musil et al., 2002; Potter, 1972) and have been combined with electrical resistivity methods (Pavoni, 2023; Wagner et al., 2019). Attempts at seismic reflection studies on rock glaciers have not been as successful (Maurer & Hauck, 2007; Musil et al., 2002). The intent of this study is to apply and evaluate seismic reflection and active-source multi-channel analysis of surface waves (MASW) to quantify the thickness and elastic properties of the debris layer on rock glaciers. If appropriate acquisition parameters are followed, the dataset for these surveys can be collected at the same time, and can also be used to pick the first-arrival times for the refraction and reflection dataset. To determine the effectiveness and accuracy of these methods, we compare the results of ground-penetrating radar (GPR) profiles taken on coincident lines, synthetic seismic shot records using a finite-difference wave propagation modeler, and the active seismic results from two glacial study sites. We use results from refraction tomography profiles to inform (*p*)-wave *a priori* values used in the reflection forward modeling and surface-wave inversion process.

1.2 Overview of Study Areas

Sourdough Rock Glacier is located in the Wrangell mountains near McCarthy, Alaska. Previous GPR surveys have confirmed that the glacier features a debris layer approximately 2.5 to 3 meters thick overlying an ice-rich core that extends up to 50 meters in depth (Meng et al., 2022; Petersen et al., 2016).

We compare active-source surface-wave acquisition parameters, processing methods, and results from Sourdough to those from a second site in the Malaspina Glacier forelands, located in Wrangell-St. Elias National Park. Malaspina Glacier is a widely studied large piedmont-style glacier in the Saint Elias mountains near Yakutat, Alaska (Russell, 1893; Sauber et al., 2005). The glacier is protected from tidal influences by a thin strip of land composed of glacial outwash deposits known as the Malaspina forelands. In certain parts of the forelands, sediments overlie large continuous masses of remnant glacial ice emplaced by past glacial activity (Gustavson & Boothroyd, 1987). This remnant ice is the target of our surveys. The active seismic data presented here was collected in the summer of 2021 at several sites as part of a larger ongoing study to quantify the spatial distribution of buried ground ice in the forelands.

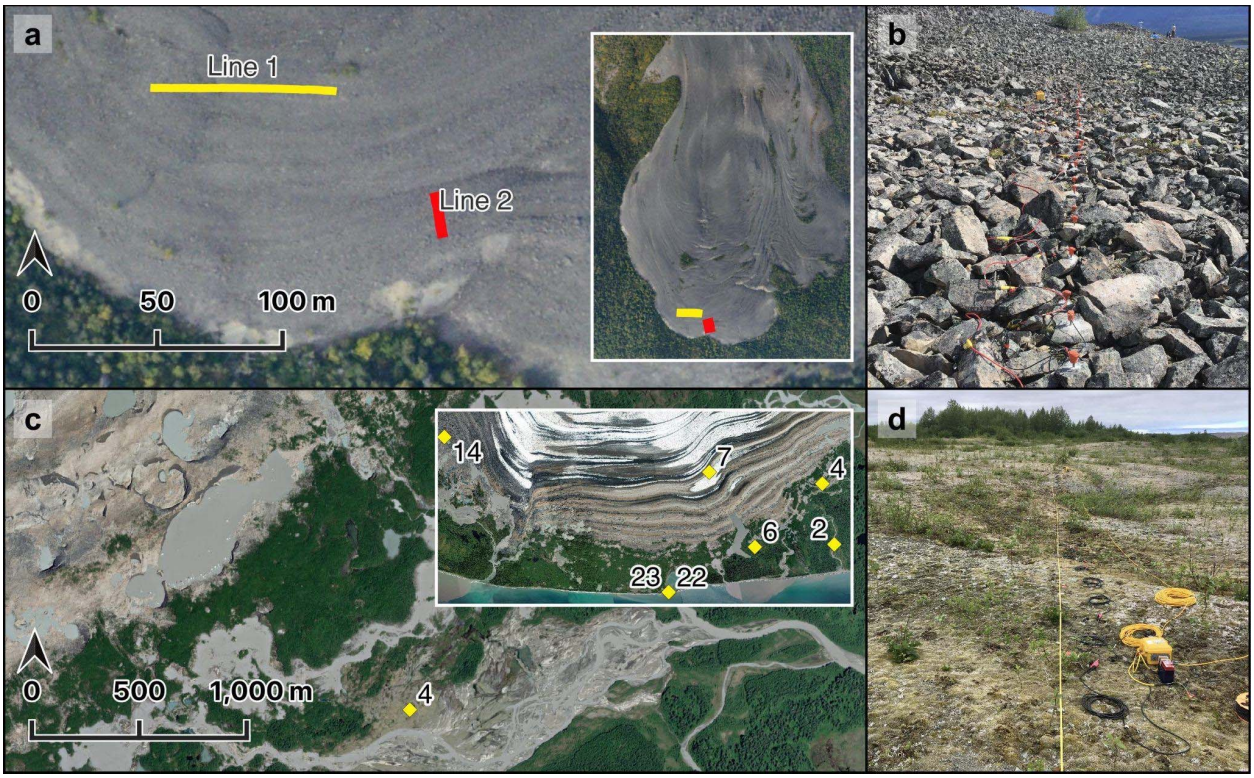

Figure 1. a) Seismic line locations near the terminus of Sourdough Rock Glacier and inlay map for full glacier context. b) Field photo of typical terrain on Sourdough Rock Glacier with geophones ground-coupled for line 1 at 0.5-meter intervals. c) Aerial image of Site 4 in the Malaspina forelands showing nearby thermokarst activity with inlay map of all sites where active seismic data was collected across the forelands. d) Field photo of the terrain at Site 4 with geophones inserted into the ground at 1-meter intervals.

1.3 Ground-Penetrating Radar Context

For a baseline comparison with the active seismic methods, we collected ground-penetrating radar (GPR) profiles along the active seismic lines on Sourdough using a Sensors &

Software PulseEKKO Ultra system operated with 200-MHz antennas. The antenna spacing was 0.5 m and traces recording received power as a function of time were collected at discrete 0.1-m intervals along the profile, allowing for the detection of the radio echo from the dielectric contrast between the debris and the ice. Using Sensors & Software EKKO_Project software, we subtracted the background average, migrated the data, and applied a depth correction assuming a velocity of 0.1 m/ns, which corresponds to a dielectric permittivity of nine. This value is consistent with debris values from GPR studies on other DCG (Meng et al.; 2022; Monnier & Kinnard, 2013; Petersen et al., 2020) and it provides a lower bound on estimated debris thickness because most lithologies do not have a dielectric permittivity exceeding nine (Campbell & Ulrichs, 1969). By picking the first break of the reflection interpreted to be the debris/ice interface, we find a minimum debris thickness of 1.5 m and a maximum debris thickness of 2.2 m along these transects (Figure 2). The uncertainty in the dielectric permittivity of the debris is the largest source of uncertainty in the GPR-derived debris thickness measurements. Due to environmental conditions and logistical constraints at the Malaspina survey sites, no GPR data were collected.

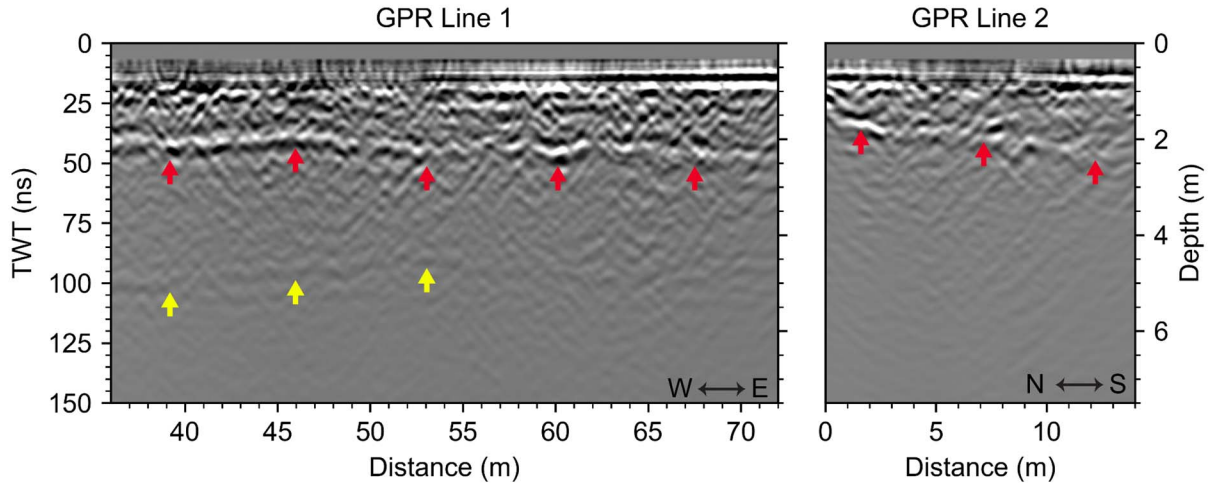

Figure 2. Surface-flattened reflection results from the 200 MHz GPR surveys coincidental with the seismic line locations. The reflection surface denoted by the red arrows is interpreted as the bottom of the loose debris layer. A second reflector likely from internal debris in Line 1 around 5 meters depth from 36 to 53 meters distance is marked by the yellow arrows.

1.4 Survey Method Background

Seismic Refraction is a well-established tool in geophysical investigations for glaciology, where the start of the seismic signal, termed the (*p*)-wave first arrivals, are picked from the trace data. The result of the picking process is a set of times (T), usually in ms, and offsets from the source location distance (X), usually in m. The T-X information can then be inverted for (*p*)-wave structure of the subsurface, and is useful for locating features such as bedrock, geological layer interfaces, or the water table. The depth of investigation depends on the velocity of the subsurface

strata, the length of the seismic array, energy of the source, and attenuation properties of the materials (Musgrave, 1967).

Seismic reflection is a widely used method in oil and gas exploration and has also been used in glacial studies to determine glacier thickness and internal geometry (e.g. Baker et al., 2003). Reflections from the layer interfaces are returned to the receiver array as a hyperbolic event, due to a phenomenon called normal moveout (NMO). The NMO velocity can be solved for by using the intercept time at zero offset and the geometry of the array (Dix, 1955). The records can then be corrected using the NMO for each reflection hyperbola event and stacked at a common depth point (CDP) to create an image of the subsurface layers (Sheriff & Geldart, 1982; Yilmaz, 2001).

Multi-channel analysis of surface waves (MASW) is a seismic exploration technique commonly used in civil engineering site characterizations. It is a useful tool to determine the (*s*)-wave properties of the geology in the upper tens of meters of the subsurface when using an active source and dense receiver spacing (Park et al., 1999, 2007). The method takes advantage of the dispersive properties of Rayleigh waves, the main component of ground roll (Richart, F.E. et al., 1970). The phase velocities at each frequency component of the Rayleigh waves can be used to yield a dispersion curve, which is inverted for a shear (*s*)-wave velocity profile of the subsurface (Park et al., 1999). In typical seismic refraction and reflection shot records, ground roll resulting from the source can be seen as a distinct cone-shaped event propagating out from the source location. Ground roll is often unwanted and filtered out of the record to identify other events of interest such as reflections (Karslı & Bayrak, 2004; Yilmaz, 2001), but MASW acquisition parameters seek to enhance the ground roll. Since Rayleigh waves can be generated using a compressive source typically used for (*p*)-wave surveys, seismic refraction, reflection and MASW surveys can use the same dataset, given that the time of the shot records is long enough to capture the whole ground-roll package at the farthest offset. The analysis assumes the wavefront is propagating as a plane wave, so the source must be offset at a far enough distance from the first receiver to approximate the needed wavefront characteristics. High-frequency surface waves are also easily attenuated so a maximum offset depending on site characteristics needs to be chosen as well (Park et al., 1999).

2 Data Acquisition

At the Malaspina Glacier foreland study sites, the active seismic surveys were optimized for refraction tomography (SRT) and MASW data collection. 24-channel Geometrics Geode exploration seismographs were used to connect linear arrays of 24 to 48 geophones at 1-meter receiver spacing intervals depending on the spatial limitations of the site. We used 4.5-Hz geophones, a standard frequency to collect active source surface-wave data (Foti et al., 2018; Park et al., 2002). A 7.25-kg (16-lb) sledgehammer was struck on a 1.9 cm (¾ inch) thick steel plate as the source. The source was not placed at every receiver station along the transect to collect a reflection profile due to timing and logistical constraints.

On Sourdough Rock Glacier, two 24-channel Geometrics Geode seismographs using 40-Hz geophones were connected to create 48-channel linear arrays. The active seismic survey lines were chosen near the terminus of the glacier, over relatively flat areas of the debris surface. Line 1 is oriented roughly east-west with spacing of 0.5 meters. Five overlapping sub-arrays of lengths of 24 meters created a total transect length of 72 meters. Line 2 is oriented roughly north-south with a total of 48 receiver stations spaced 0.3-meters apart that span a total distance of 14.4 meters (Figure 1). We used a recording sampling rate of 0.063 ms. At line 1, five shots were repeated at each source point to enhance the signal to noise ratio. For line 2, 10 shots per source point were collected.

The purpose of using higher frequency geophones on Sourdough was primarily to collect shallow reflection data at high frequencies (Brabham et al., 2005; Steeples et al., 1997), though we also use the dataset for MASW. A study by Park (2002) detailed the use of higher-frequency geophones for MASW and found that a reliable dispersion curve was still attainable and the receivers were able to record at frequencies lower than 10 Hz, though it does limit the investigation depth depending on site characteristics. Since the aim of our surface-wave study was the upper few meters of the subsurface, we found this acceptable in order to simultaneously carry out a reflection survey.

A 7.25 kg (16-lb) sledgehammer and a standard 0.63 kg (22 oz) geologist's rock hammer were used as sources during acquisition. The varying shape and size of the surface debris on Sourdough ruled out the possibility of using a steel plate as an impact surface for the source because of inadequate coupling, resulting in the plate bouncing after being struck. Since using an impact surface was not possible, the source was struck directly on debris-clasts at each shot point. Most of the surface rocks are loose and platy, which resulted in debris movement, breakage, and flyrock after sledgehammer strikes, producing unwanted events in shot records. During acquisition, shot records with obvious effects from these events were not kept after visual inspection.

After some time in the field, it became evident that shots recorded with the rock-hammer source yielded better field efficiency, less source-generated noise, and more shots could be stacked at a particular shot location. For those reasons, only the rock hammer was used for reflection acquisition on the last half of Line 1 and the whole of Line 2, with shot locations at every receiver station. The heavy sledgehammer was then used at either end of the arrays to generate forward and reverse shots used for MASW, because the observed surface-waves were stronger than those generated by the rock hammer.

To couple the receivers to the debris surface, geophones with spikes were placed in 0.95 cm (⅜ inch) diameter holes that were drilled into debris clasts using a cordless hammer drill (Figure 3). This method of coupling was chosen because it allowed for precise positioning of geophones on the survey line and allowed for the minimization of geophone tilt (Maurer & Hauck, 2007). Each receiver was geo-located using a multi-band RTK GNSS receiver with centimeter precision at the top of the geophone. The approximate height each geophone sits above the surface,

9 cm, was subtracted from the elevation values at each station to infer a topography profile for the top of the debris layer.

Figure 3. Method for geophone coupling to individual debris clasts after Maurer & Hauck (2007).

3 Processing & Results

3.1 Refraction Tomography

To pick the first arrival times, we normalize the shot traces and manually pick the data. The first arrival times for the Malaspina sites were easily identifiable and required no filtering to pick other than gain-setting manipulation. In the Sourdough records however, the p-wave first arrivals (the seismic wave traveling along the surface of the debris) is obscured by the air wave (sound of the hammer hitting the surface) at short offsets (0-5 m) (Figure 4). In these records, the airwave has a much higher frequency content and lower amplitude than the first arrivals, so the two can be distinguished to pick a reliable first arrival time for the debris layer. The Sourdough records are also associated with more source-generated noise, so traces and records that could not be reliably picked were avoided and clean records were used for the tomography inversion.

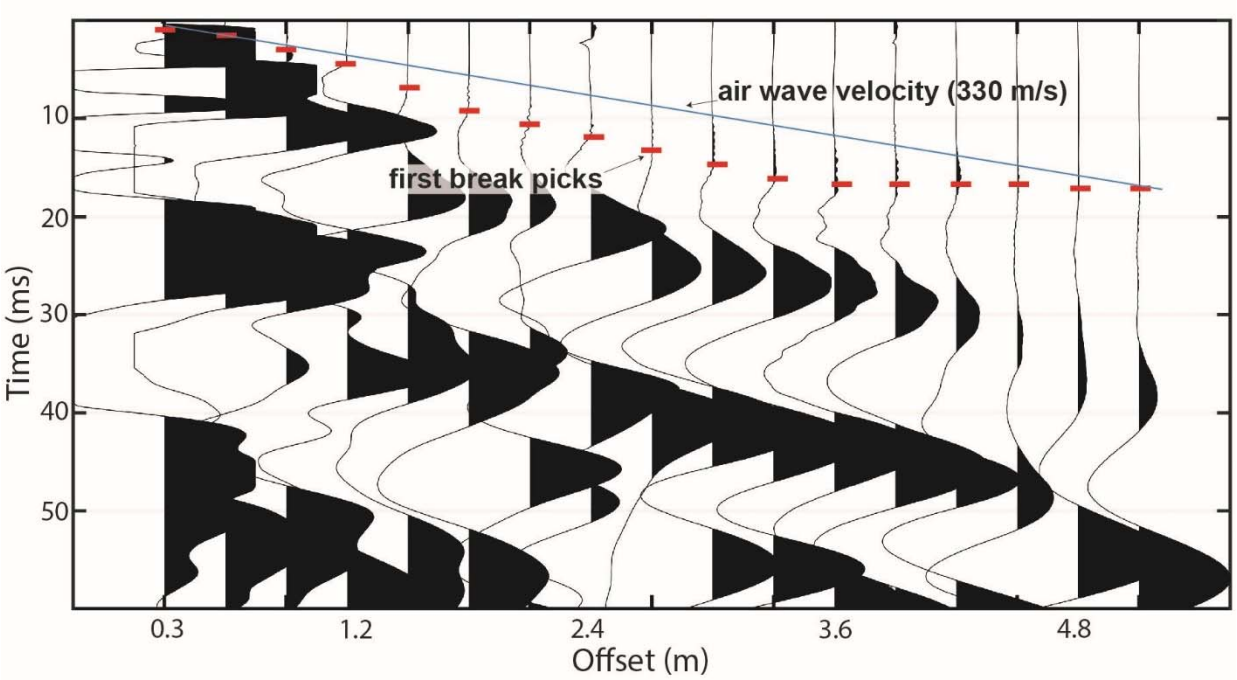

Figure 4. An example shot record from Sourdough Line 2 for near-offset receivers. The first arrival p-wave (red dashes) is obscured by the air-wave which is represented by the line having a slope of 330 m/s and recognized by high-frequency low-amplitude arrivals.

To invert the refraction data, we use the python Geophysical Inversion Modeling Library (pyGIMLi) (Rücker et al., 2017) which uses a shortest-path algorithm (Heincke et al., 2010; Ronczka et al., 2017) to calculate seismic energy as ray paths from the modeled velocity structure. The inversion scheme requires a data weight for each travel-time pick, which we assign as a linear function based on source-receiver offset used in other shallow refraction tomography studies, where error increases with offset (Flinchum et al., 2022).

We assign a minimum picking error for the Malaspina foreland records of 0.5 ms and a maximum error of 2 ms. The Sourdough shot records have a much lower signal-to-noise ratio, so we assign a minimum picking error of 1 ms and a maximum of 3 ms. The values of these errors were assigned based on standard deviation from the mean pick time of a representative shot record for close and far offsets.

Tomography results from the refraction first breaks at sites 2, 6, 14, 22 and 23 in the Malaspina forelands do not indicate any shallowly buried remnant glacial ice, which has a typical (*p*)-wave velocity range of 3600-4000 m/s (Baker et al., 2003; Press, 1966) when free of any entrained debris. These sites indicate slow velocities (100-800 m/s) in the upper few meters and maximum velocities around 2000-2800 m/s. The slower range is consistent with observed velocities for dry or well-drained sediments or gravels and the upper range with saturated and more consolidated sediments and tills (Press, 1966; Uyanık, 2011). Tomography sections for these sites and their corresponding inversion statistics can be found in Appendix A. We do observe a large

velocity contrast around 14 meters in depth at Malaspina Site 4 (Figure 5), which we use as a comparison to the Sourdough sections as this velocity contrast is consistent with expectations for glacial till over massive ice.

The inversion results for Malaspina Site 4 (figure 5) achieve a χ^2 value of 0.489 and an RMS of 1.243ms after 15 iterations. χ^2 is a statistical measure of the observed and expected values and RMS or root mean square is the standard deviation. Materials with (*p*)-wave values in the accepted ice-velocity range are observed around 14 meters in depth. Depth to bedrock in the Malaspina forelands has been previously estimated to be in excess of 150 m (Allen & Smith, 1953), strongly ruling out the likelihood of a bedrock refraction in the upper 20 m and strengthening the case for massive remnant glacial ice. The tomography results show higher velocities than typical massive glacial ice (>4000 m/s) at the bottom of the mesh. It should be noted that the modeled ray coverage density is not as populated as the top and middle of the mesh, which makes us less certain of the results. We interpret the overlying strata of debris at this site to range from dry, well-drained gravel near the surface, to more consolidated wet sands and clays starting at 5-m depth.

For the Sourdough lines, after 15 iterations we achieve a χ^2 value of 1.12 and an RMS of 1.02 ms for line 1 and a χ^2 value of 0.469 and an RMS of 1.848 ms for line 2 (Figure 5). The loose debris layer ranging from 1.5 to 2.5 meters depth is characterized by a (*p*)-wave velocity around 185 m/s but shows increases towards 1000 m/s toward the interfaces with the ice core. Our observed velocity for the very shallow debris layer (0 to 1 m depth) differs significantly from previous refraction studies done on DCG, where velocities around 500 m/s have been observed for the debris mantle (Bucki et al. 2004; Pavoni et al., 2023), though 300 m/s has been observed as well (Pasquale et al., 2022). Our study differs from the ones noted here in the receiver spacing, where the other studies used 3 to 15 m, whereas we used 0.5 and 0.3 m on Sourdough and 1 m at Malaspina, allowing us to characterize the debris layer velocity as gradational and highly variable. The observed 185 m/s direct wave velocity at near offsets represents the complicated path the direct arrival has to take to the geophones. The cobbles that make up the debris individually have a p-wave velocity in the range of granitic rocks (5000-6500 m/s), but the odd coupling between cobbles and large void space between them complicates the path the direct wave has to take significantly, but for farther offsets the ray paths are able to travel in more consolidated materials.

The depths of the modeled velocities agree with the interfaces indicated by the GPR profiles (Figure 2). A thin layer beneath the loose debris with velocity values between the loose debris and pure ice values is interpreted as an ice-cemented debris-layer. Velocities approaching near pure-ice values are modeled starting at 3.5 m depth for Line 1 and 4.5 m for Line 2. The modeled ray paths for Line 2 extend deeper than those for Line 1, even though the array length is shorter. This could be due to discontinuous ice-rich zones and a thicker ice-cemented debris layer, which would not provide a sharp layer interface for the refracted wave to travel along, as observed for Line 1. Picking the airwave as the first arrival instead of the direct wave results in a debris layer thickness of roughly twice the GPR-derived thickness, further confirming that these arrivals are indeed the arrival from the air wave.

We assign layer properties used for the reflection forward modeling and as *a priori* values for the inversion of the surface-wave data using observed values from the refraction tomography results and studies on other glaciers cited in Table 1. The table is a simple 4-layer model interpretation of the overall glacier structure and does not consider internal variations of compaction within the debris layer, the likely presence of partially ice-cemented debris near the surface, or internal debris in the glacier core.

	Vp (m/s)	ρ (g/cm³)	h (m)	Notes
L_1	185±15*	1.85±0.1†	1.5-2.5	*Slope of direct-wave first arrivals ; †Calculated using debris clast density of 2.65g/cm³ and estimated layer porosity of 0.3 (Anderson & Anderson, 2018) and the bulk density equation§
L_2	1600±400*	1.6±0.1†	1-2	*from observed data ; †Average density of permafrost (Kawasaki et al., 1983)
L_3	3650±150*	0.95±0.05†	12-30	*clean glacial ice velocity from observed data and previous studies (Kohnen., 1974; Press, 1966) ; †Density of glacial ice (Shumskiy, 1960)
L_4	4800*	2.65†		*†meta-sedimentary bedrock estimations (Press, 1966)

Table 1. Sourdough Rock Glacier layer properties for the loose debris (L_1), interpreted ice-cemented debris (L_2), ice-rich core (L_3), and bedrock (L_4) using the observed refraction data and values from the literature. A range of observed thicknesses (h) from the refraction data and ground-penetrating radar measurements. §$\rho_b = (1-f)\rho_s$ where ρ_b is the bulk density, f is the porosity, and ρ_s is the particle density.

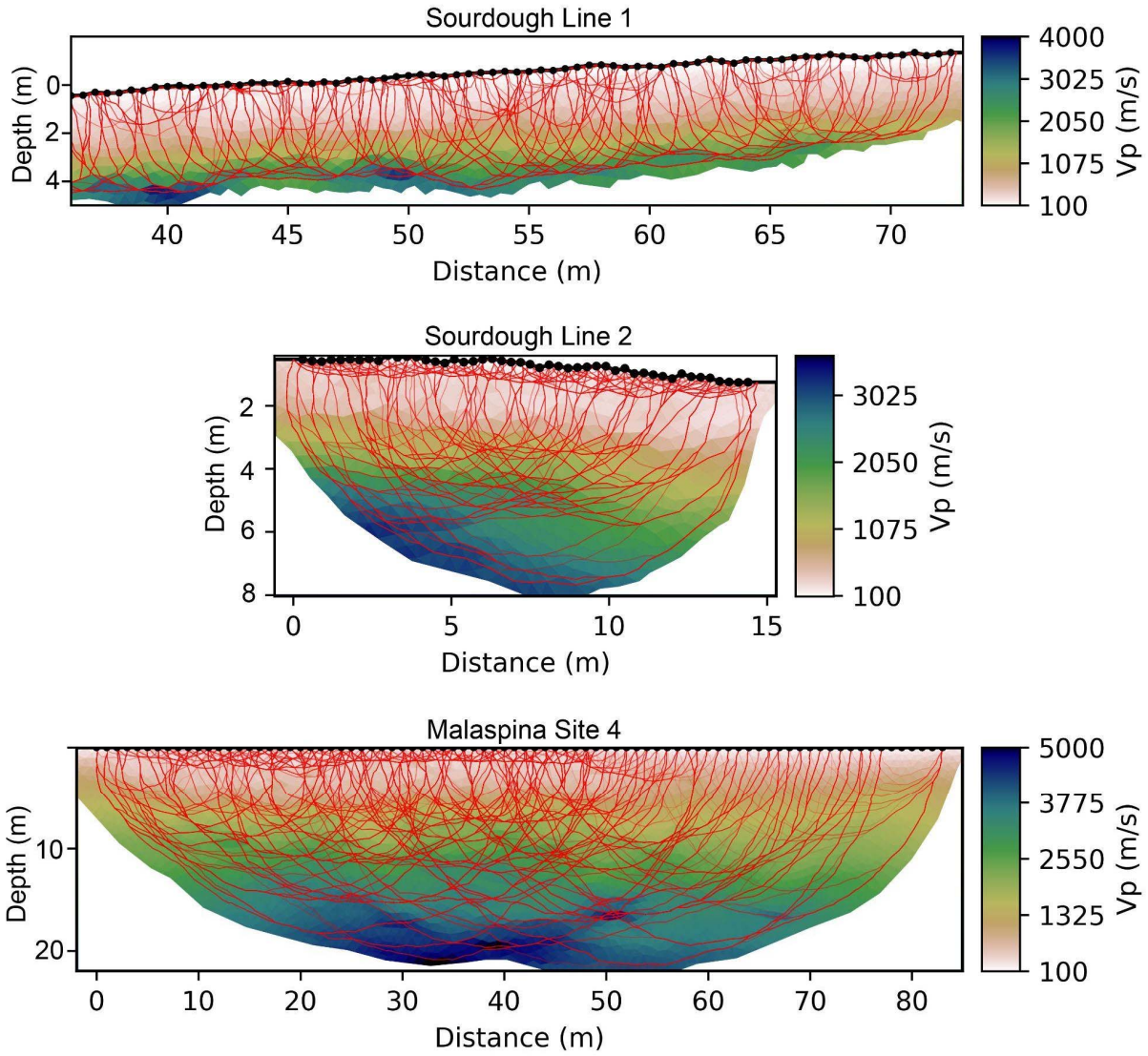

Figure 5. Results from the refraction tomography inversions for Sourdough Line 1 (top), Line 2 (middle), and Malaspina Site 4 (bottom). Modeled ray paths are drawn in red with paths associated with multiple rays brighter than paths associated with fewer rays. Receiver locations are shown as black dots.

3.2 Reflection

3.2.1 Reflection Processing

For Sourdough reflection processing, individual shot records taken at each station were stacked by source location and elevation statics were applied using the replacement velocity of 185 m/s observed from the first p-wave arrival times to account for the elevation differences between the receivers. Spectral analysis of the individual stacked records shows relatively low

frequencies (Figure 6) for both lines although the frequency response of Line 2 returns higher frequencies than Line 1 due to the smaller receiver spacing and smaller total array length of the line. Still, the majority of the recorded frequencies occur below 100 Hz and visual inspection of the stacked shot records and common depth point (CDP) gathers at high frequencies confirm that no reflections can be identified when filtering for frequencies above this value for both lines.

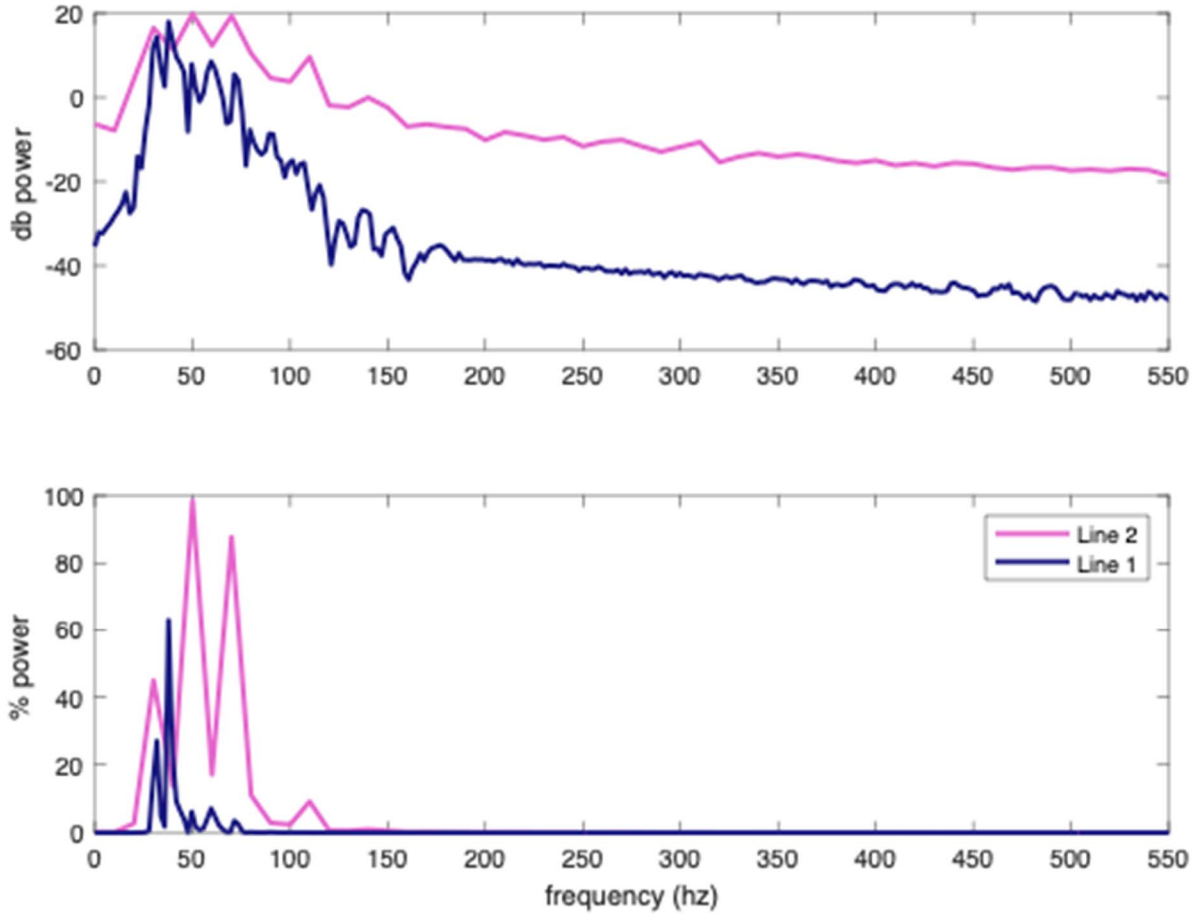

Figure 6. Frequency content of the recorded signal from an example record from Line 1 (0.5 m receiver spacing, total length = 24 m) and Line 2 (0.3 m receiver spacing, total length = 14.4 m).

Using a bandpass filter with corner values at 16-24-140-180 Hz, a reflection hyperbola can be picked around 21 ms in the high-fold CDP gathers for Line 1 and around 22 ms for Line 2, both characterized by a normal move-out velocity of 185 ±15 m/s (figure 7) which becomes asymptotic to the direct wave. Implementation of a minimum-phase spiking deconvolution filter with a white noise level of 0.1 was found to increase the resolution of this event and decrease the associated multiple energy. Additional processing steps included surgical muting to eliminate ground roll and direct-wave energy. Automatic gain control was also applied.

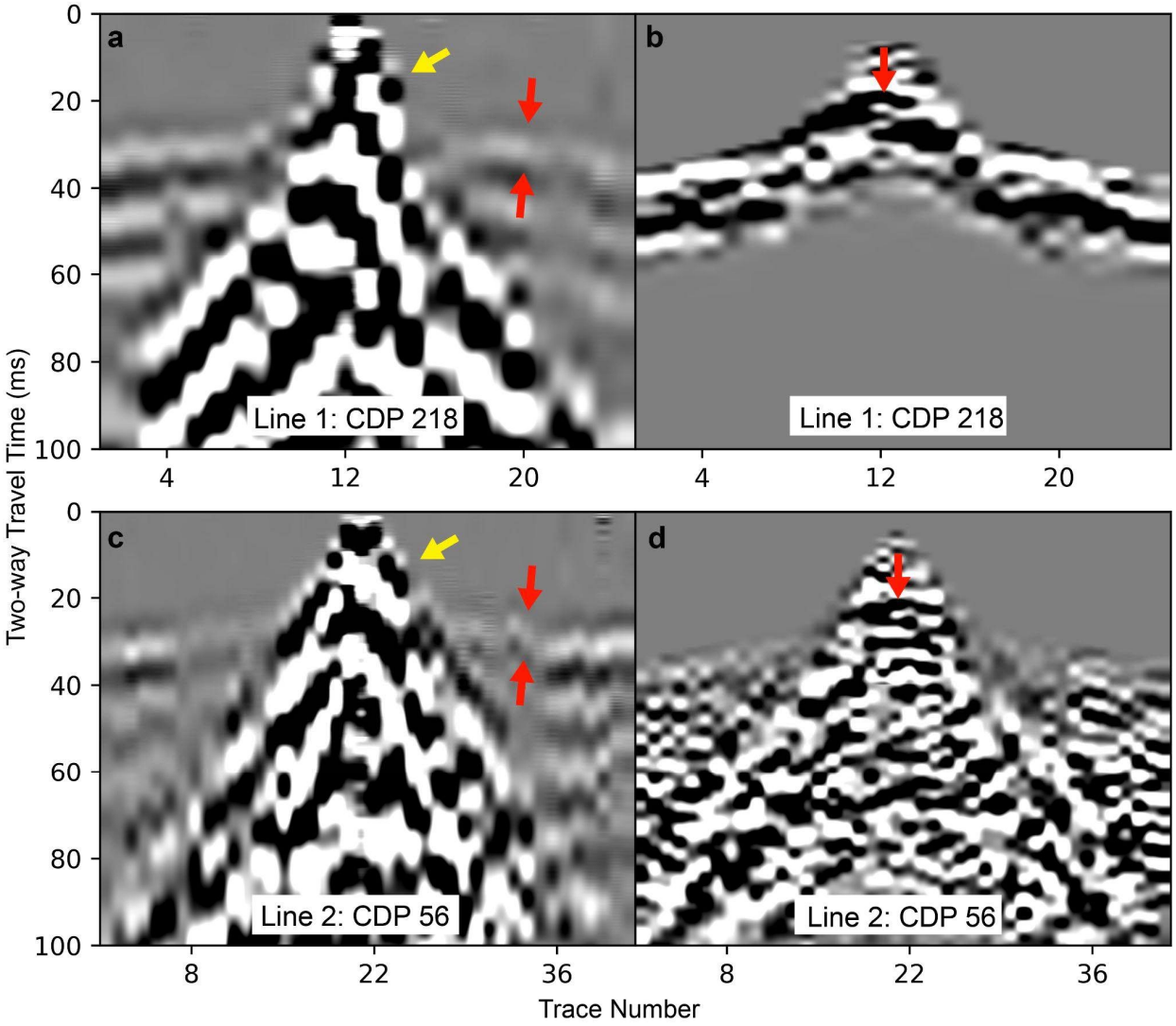

Figure 7. (a) Raw CDP gather for Line 1 CDP bin #218 with the direct wave denoted by the yellow arrow and the refraction first-arrival wavelet denoted between the two red arrows. (b) after processing and muting the first-arrival energy. (c) Raw CDP gather for Line 2 CDP bin #56 with the same notation as (a). (d) after processing and muting the first-arrival energy. A weak reflection hyperbola indicated by the red arrows can be picked in (b) and (d) with a normal move-out velocity of 185 m/s ±15 m/s. The SEGYIO python software was used to generate the figure.

3.2.2 Synthetic Generation

To accurately interpret and pick reflection hyperbola in the Sourdough field records, we generate synthetic shot records based on expected velocity structures for both lines. To do this, we use the finite-difference wave propagation modeler SPECFEM-2D (Komatitsch, 1997; Komatitsch et al., 1998; Xie et al., 2014) and the layer properties defined in Table 1 to generate the models

depicted in Figure 8. The synthetics generated off of these models used the same receiver geometry as our field data. Model 1 and Model 2 are simplified representations of the expected structure based on the GPR results and observed and expected seismic velocities from Table 1. Model 3 exaggerates the ice thickness of Model 1 to see if a signal from the glacier bed influences the trace data. If a signal from the glacier bed is influencing the synthetic record for Model 1, we should observe a change for Model 3, as the bed response would occur at a much later time. The wave propagation parameters assume no attenuation factors. The center frequency of the source is evaluated at 100 Hz (the frequency of the observed first arrival wavelet in the field records shown in Figure 4) and 500 Hz, which allows for easier visual separation of refraction and reflection events.

It should be noted that while the synthetic models have a shear-wave velocity assigned to each layer, they do not accurately represent the complex shear-wave variations within the debris. Therefore, the ground-roll Rayleigh waves are not adequately duplicated in the synthetics and an analogous surface-wave package cannot be picked. Due to this limitation, we use the synthetic shot records as a comparison for potential reflection events only and not for synthetic comparison to the field surface-wave data in the MASW inversion process.

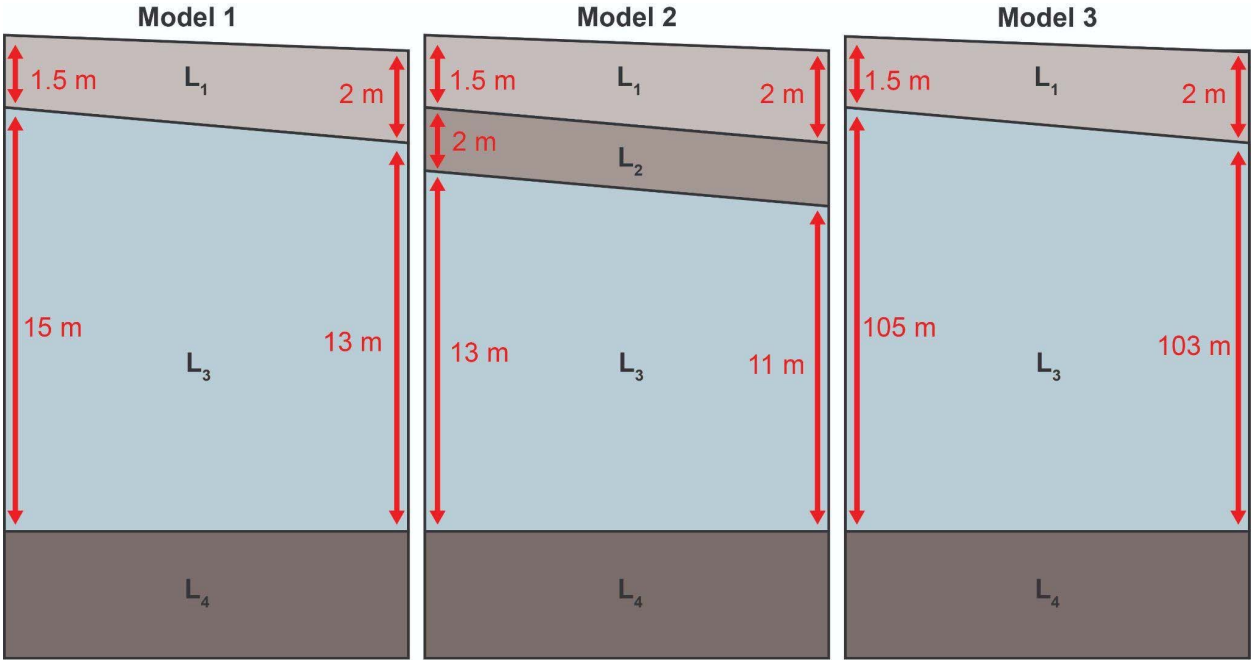

Figure 8. Representation of the simplified glacier structures used in the synthetic forward modeling of Sourdough Line 2. The (*p*)-wave and density values for the corresponding layers are listed in Table 1. The geometry of the loose debris layer (L_1) and ice-cemented debris layers (L_2) are from the GPR and refraction tomography observations. The length along the model corresponds to the array length of Line 2.

No reflection hyperbolae were visually detectable at later times associated with deeper interfaces, such as an ice-cemented debris layer or the glacier bed. Figure 9 compares the results from the synthetic shot records to the field data. Our recorded frequencies show that no discernible reflections can be picked in the unstacked field records, which we replicate in the 100 Hz synthetics. The synthetic models at 100 Hz visually match the observed data fairly well, though Model 2 produces a better match for the farther-offset events noted by the red boxes, possibly due to the presence of a thin ice-cemented debris layer. There are differences in the first arrivals between the synthetics and field data, a result of the non-planarity of the layer interfaces and lateral changes in dip angle, which we could not capture. However, the simplified synthetic structure provides a general analog to the field data.

The lack of an observed bed reflector in the synthetic models can be explained by the reflection and transmission coefficients of the debris-ice interface (Sheriff & Geldart, 1982). Reflection and transmission coefficients are strongly affected by the difference in acoustic impedance (a product of layer density and seismic velocity) of each geologic layer. Table 2 lists the reflection coefficients for Models 1 and 2 at normal-incidence of a pure-elastic medium using the layer properties from Table 1. In both models, the debris layer has a very strong reflection coefficient (Model 1 R_{mean} = 0.81; Model 2 R_{mean} = 0.749), which prevents source energy from transmitting to deeper layers as well as the transmitted energy from returning to the surface, which is below 5% for both models. These calculations do not include attenuation effects from scattering, geometrical spreading or non-normal incidence, which would decrease the amount of returned energy even further. This could explain why a deeper reflector, like the one marked by the yellow arrows in the radar profile (Figure 2) or a glacier-bed reflection does not appear in the individual seismic shot records or CDP gathers.

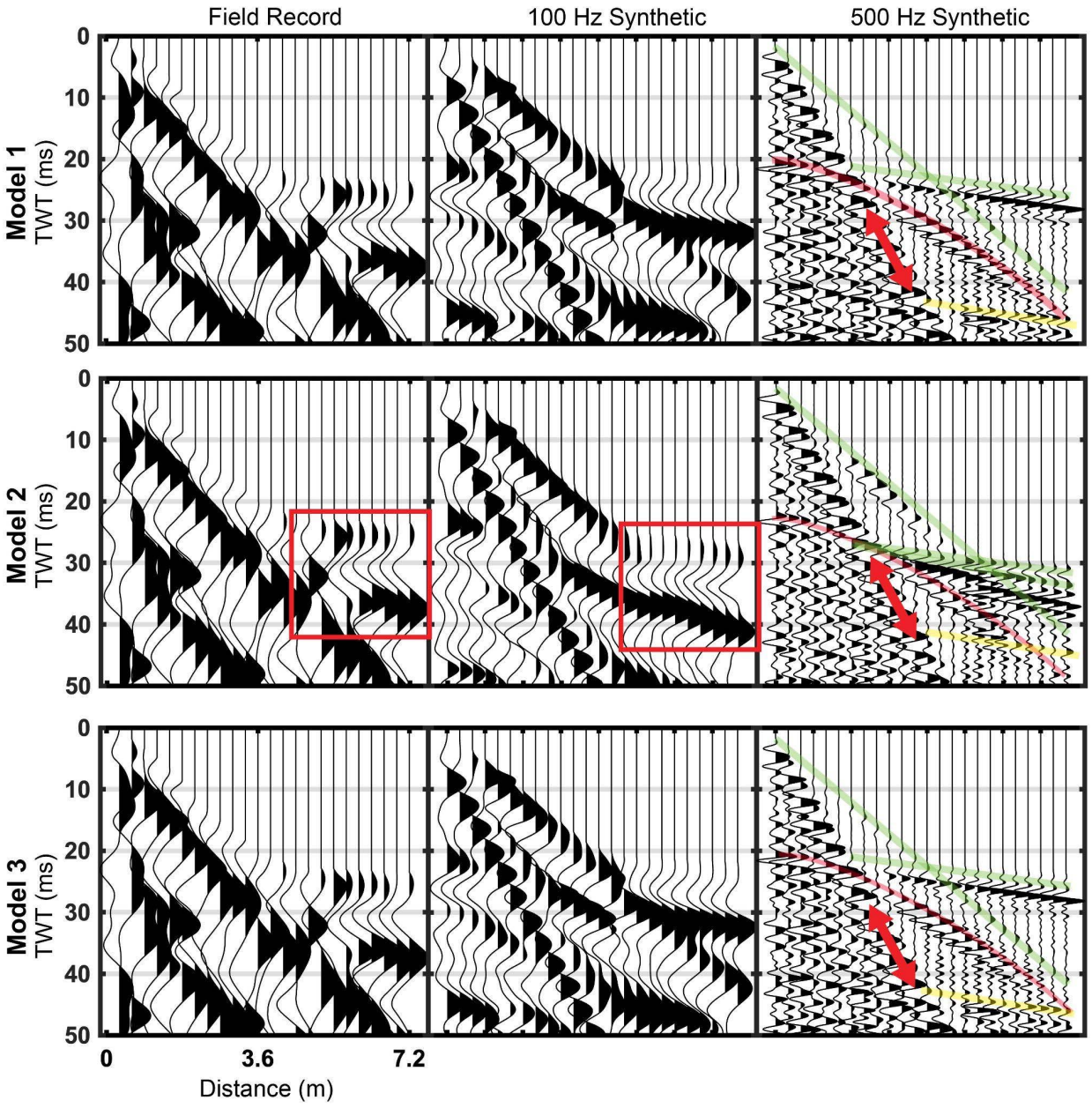

Figure 9. Line 2 Field record (ffid 3255) and synthetic record comparison of model 1 (top), model 2 (middle), and model 3 (bottom) parameters. The direct wave and refraction events are highlighted in green, the bottom of the debris layer reflection hyperbola in red, and refraction multiple in yellow. The red double-sided arrow marks the strong surface wave event in the debris layer that does not match the field data. The better visual match between the Model 2 far-offset events and the field data is outlined by the red boxes.

Model 1 & Model 3 Layer Parameters

Layer Properties	Interface	R_{mean} ; T_{mean}	Coefficient Range	% Returned to Surface
$L_1 = V_{p1}(185\pm15);\rho_1(1.85\pm0.1)$ $L_2 = V_{p2}(3650\pm150);\rho_2(0.95\pm0.05)$	L_1 / L_2	0.81 ; 0.19	±0.03	81±3%
$L_3 = V_{p3}(4800);\rho_3(2.65)$	L_2 / L_3	0.552 ; 0.448	±0.033	2.2±0.77%

Model 2 Layer Parameters

Layer Properties	Interface	R_{mean} ; T_{mean}	Coefficient Range	% Returned to Surface
$L_1 = V_{p1}(185\pm15);\rho_1(1.85\pm0.1)$	L_1 / L_2	0.749 ; 0.251	±0.07	74.9±7%
$L_2 = V_{p2}(1600\pm400);\rho_2(1.6\pm0.1)$ $L_3 = V_{p3}(3650\pm150);\rho_3(0.95\pm0.05)$	L_2 / L_3	0.162 ; 0.838	±0.148	1.62±1.58%
$L_4 = V_{p4}(4800);\rho_4(2.65)$	L_3 / L_4	0.552 ; 0.448	±0.033	3.6±2.4%

Table 2. Reflection (R_{mean}) and transmission (T_{mean}) coefficients at normal-incidence to the source for the pure-elastic simplified velocity structures modeled in the synthetic shot records (Figure 8) using the Zoeppritz equations (Sheriff & Geldart, 1982). (*p*)-wave velocities are in m/s and densities in g/cm^3. The amount of source energy returned to the surface is very high for the bottom of the debris layer and negligible before attenuation effects from deeper layers.

3.2.3 Reflection Results & Interpretation

Figure 10 shows the stacked CDP depth sections for the Sourdough reflection surveys. The sections were migrated to depth sections using a velocity of 185 m/s picked from the reflection hyperbolas in the CDPs discussed earlier. The first half of Line 1, for which the source was the 16-lb sledgehammer, yields no reliable reflector and is not imaged in the final results. The lack of a reflector for this portion of the line is probably a result of the signal-to-noise ratio, with much more source-generated noise associated with shots taken with the sledgehammer versus the rock hammer. The last half of Line 1 from meters 37 to 72, where the rock hammer was used as a source, yielded better results. The imaged reflector is interpreted as the bottom of the loose debris layer and agrees with the picked reflector from the coincident GPR data. The closer receiver spacing for Line 2, yields a stronger reflector from the bottom of the loose debris layer and lateral variability of the interface depth is more apparent. Comparing the seismic reflection results to the GPR results (Figure 9), it is apparent that the GPR yields more coherent data, as there is a higher signal to noise ratio than the seismic data. It is encouraging that the picked seismic reflection for the bottom of the loose debris closely matches the behavior of the interpreted reflection from the GPR data.

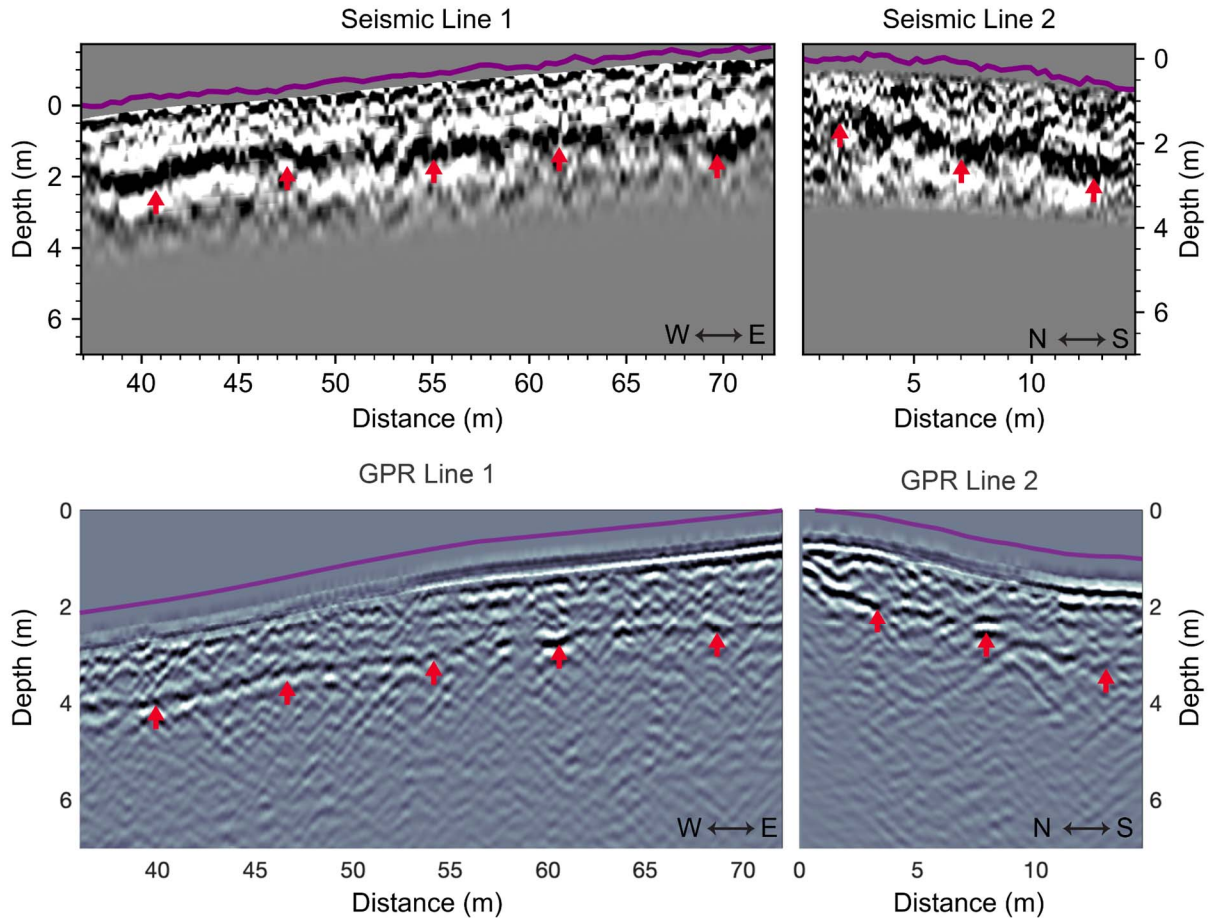

Figure 10. (Top) Seismic Line 1 and Seismic Line 2 processed and stacked CDP sections from the Sourdough glacier reflection surveys converted to depth. The reflector denoted by the red arrows is interpreted to be the bottom of the loose debris. The purple line indicates the approximate topography of the debris surface from GPS data collected at each receiver station and corrected for geophone height. Depth = 0 is relative to the surface at the first receiver station in each line. (Bottom) The GPR results are corrected for topography and displayed for comparison, with the red arrows denoting the bottom of the loose debris. Differences in the topography line are a result of using a Topcon SGR-1 DGPS for the PulseEKKO GPR system and a RTK GNSS receiver for the seismic geophone locations, which is described in section 2.2.

3.3 MASW

3.3.1 MASW Processing

Preliminary MASW processing included stacking multiple individual shot records by source location and applying a surgical mute to isolate the surface waves. The complex velocity structure of the debris layer on Sourdough necessitates custom muting for each stacked shot record to accurately isolate the surface waves, while general mutes based on offset could be used for Malaspina Site 4. A bandpass filter fitting the frequency spectrum of each site was also applied.

The corner frequencies used for the Sourdough lines are 2-4-50-80 Hz. The Malaspina site used a bandpass filter with frequencies of 2-4-100-120 Hz.

A minimum offset of 5.5 m was used when selecting traces for the analysis on Sourdough to account for near-field effects of non-planar wave propagation. After visual analysis of dispersion-image coherence, it was determined that a maximum offset of 18 m could be used for trace selection. Incorporating traces at larger offsets greatly reduced the quality of the dispersion image. For the Malaspina site, a minimum offset of 6 m was used, while the full line length to 53-m offset was used as the attenuation effects were much less than for the Sourdough data.

To extract the experimental dispersion curve from the shot records, the software MASWaves (Olafsdottir et al., 2018) was used. MASWaves applies a Fourier transform to the trace data, normalizing for each phase velocity and wavelength set, and summing the set amplitudes to create a dispersion image (Figure 10). The experimental dispersion curve was then manually picked from the peak values of the dispersion image. We then inverted the picked fundamental mode of the dispersion curve to yield a 1-dimensional shear-wave (Vs) velocity profile in the MASWaves software. A limitation of MASWaves is that higher modes of the dispersion image are not able to be accounted for in the inversion process. A multi-modal inversion process could lead to more accurate results and a larger depth of investigation.

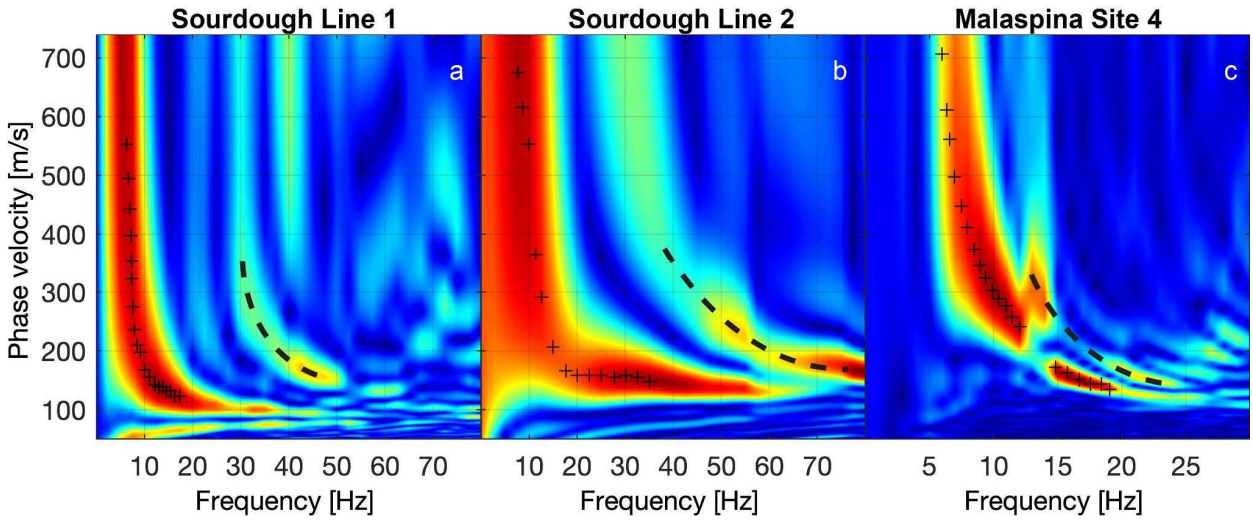

Figure 11. Examples of normalized amplitude dispersion spectrum images from Sourdough Line 1 (a), Line 2 (b), and Malaspina forelands Site 4 (c). The picked fundamental mode of the dispersion curve is marked with black crosses and identified strong first higher modes as dashed black lines.

3.3.2 MASW Results & Interpretation

Examples from Sourdough indicate that with close receiver spacing and source offset limited to a maximum of 18 m, a reliable and clean dispersion curve can be extracted from the

surface-wave package. The Sourdough curves display strong frequency amplitude below 10 Hz (Figure 11a,b) even with 40-Hz geophones. The curve for Line 2 is smoother compared to Line 1, indicating that closer receiver spacing leads to a more defined curve, although this could also be due to differences in velocity structure, as the debris cover is a laterally complex medium. The fundamental mode of the Malaspina site shot record displays a jump to the first higher mode around 12 Hz and a sharp step back down to the fundamental mode around 16 Hz (Figure 10c). This break to a higher mode indicates that the surface-wave energy is influenced by a sharp velocity contrast at depth. The extracted Sourdough dispersion curves do not display a break to a higher mode at low frequencies, likely indicating that the surface waves are not traveling through an interface with high velocity contrast as we expect for the debris layer and ice-rich glacier core.

Figure 12(a,b) shows the results from the fundamental mode inversion of the modeled velocity structure at Malaspina Site 4. The best fit for layer model 1 which uses Vp, Vs, and ρ parameters analogous to a till debris layer which compacts with depth over a till halfspace at 14-m depth has a normalized root-mean-squared error (NRMSE) of 92%. The error for model 2, which uses the same thickness, Vp, Vs, and ρ parameters for the debris layer as model 1, but incorporates parameters for an ice-rich half-space at 14 m depth is 2.4 %. From this we conclude that the extracted dispersion curve for this Malaspina site depends heavily on surface waves from an ice-rich layer depth.

Figure 12(c,d) displays the inversion for an example record from Sourdough Line 1. The best-fitting Model 1 parameters are analogous to an ice-cemented debris half-space starting at 2.5 m depth and Model 2 adds parameters analogous to an ice-rich half-space at 3.5 m depth. The NRMSE for Model 1 is 5.7 % and the NRMSE for Model 2 is 8.5 %. From these errors, it can be concluded that any surface waves being generated in the ice-rich core are not affecting our observed fundamental mode. As we noted earlier, a full-waveform analysis and multi-modal inversion scheme could provide a higher depth of investigation.

Sourdough Model 1 indicates that the surface waves are very sensitive to the complex velocity structure within the debris and ice-cemented debris layers. The 5-layer model shows that the debris layer can be characterized by an (*s*)-wave range of 30-160 m/s. The model supports an increase to an (*s*)-wave velocity of 680 m/s at 2.5 m depth, which is below the typical permafrost (*s*)-wave range of 1000-1650 m/s and massive ice range of 1550-2050 m/s (Killingbeck et al., 2018; Press, 1966; Tsoflias et al., 2008; Yang et al., 2011). This could indicate that at 2.5-m depth there is some ice-cementation but voids or melt could also be present.

The results for the MASW inversions are consistent with a sharp transition to high-purity ice at approximately 14 m depth at the site in the Malaspina forelands. It supports the previously discussed observations that the debris layer on Sourdough is laterally elastically complex, but ultimately gets more consolidated with depth.

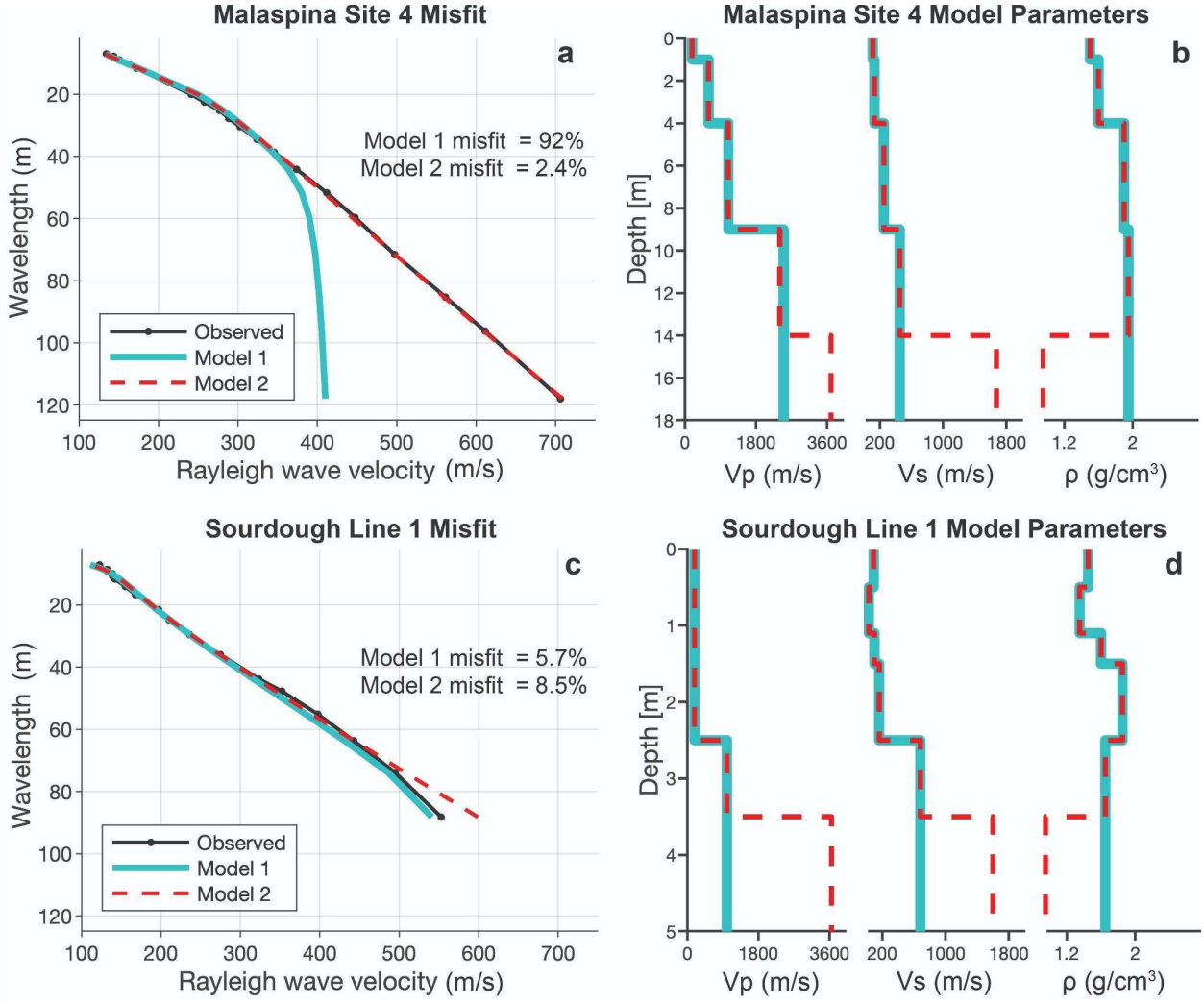

Figure 12. Results of the fundamental-mode inversion process for Vs models analogous to an ice-rich halfspace (red dashed line) and an ice-cemented debris halfspace (blue). The observed dispersion curve is plotted in black in (a) and (c) against the models. The forward model input parameters Vp, Vs, and ρ are plotted in (b) and (d).

4 Discussion & Conclusions

The primary goal of this study was to image the shallow debris-ice interface of DCG using active seismic methods and to yield more useful information from the seismic record than just the refraction first arrivals. Previous exploration studies using active seismic methods have so far been limited to refraction analysis, but we demonstrate that ultra-dense arrays generate more high-quality information for extraction from the seismic shot records, and the methods can be useful for characterizing the elastic parameters of the very shallow subsurface of these glaciers.

While GPR offers advantages over active seismic methods in terms of field logistics and quality of the results for imaging reflections, the results from the surface-wave survey are intriguing from the perspective of characterizing the elastic properties of the debris layer. The

depth of investigation for surface-wave methods is heavily dependent on energy of the source and the physical properties of the debris. Depths of investigation in the range of tens of meters can be achieved on sites with consolidated debris cover similar to the Malaspina forelands site, while the investigation is limited to only the upper few meters on loose debris surfaces such as the Sourdough site. Future studies implementing higher modes during the MASW inversion process could provide elastic parameters of the deeper subsurface. Logical next steps could provide joint inversions between 2D MASW results and p-wave refraction tomography to get a Vp/Vs ratio image could further constrain zones of consolidation or void space within this layer. When combined with electrical resistivity surveys, this could help the interpretation of void space, zones of melt in the debris layer, snow compaction within the debris and debris entrainment within the ice.

While we are able to image a reflection from the survey on Sourdough, it is apparent that GPR methods can provide more reliable and precise reflection measurements due to the frequencies involved and the higher signal to noise ratio of the acquired data, allowing it to have the ability to image the deeper reflections in the subsurface on these glacial features. Shortfalls of the GPR method though are the uncertainty in the dielectric permittivity of the debris and an assumed velocity for the whole section. In this regard seismic methods can provide insight, as the velocities are observed from the data, which reduces uncertainty in the interpretation. We were able to image a reflection from the bottom of the loose debris layer, which was the primary goal of the reflection work on Sourdough. Secondary goals of imaging deeper reflections were not successful, which we explain by the fundamental acoustic properties of the velocity structure and synthetic record comparison. We observe that high-frequency filtering, typically above 400 Hz for ultra-shallow reflection processing (Steeples & Miller, 1998), is not possible with reflection data collected on debris-covered glaciers and rock glaciers due to the highly attenuating nature of the debris layer. Most of the recorded frequency values occur in the 20-60 Hz range and no coherent signals appear in the individual shot records or CDP gathers when looking at high frequency-filtering windows.

Future surveys investigating the shallow structure of debris-covered glaciers could be designed using distributed acoustic sensing (DAS). As we have shown, results can be achieved with very small receiver spacings, which makes DAS a logical next step since measurements can be recorded at any point along the fiber optic cable. DAS uses Rayleigh backscattering from a laser impulse to record vibrations or changes along a fiber optic cable (Kingsley, 1986) generated by a source at any point along the cable. While field efficiency for active seismic DAS surveys would be much greater than setting up a traditional geophone array like this survey uses, further work to understand the coupling between a DAS cable and the debris surface would need to be examined, although preliminary work (Spikes et al., 2019) indicates that coupling of fiber optic cables would be sufficient for such investigations.

Acknowledgements

This work was funded by The University of Arizona and National Science Foundation Grant 1929577. We thank Wrangell- St. Elias National Park for the permit to carry out field research in Malaspina Glacier and Mike Loso of the NPS for his field coordination efforts. We thank our colleague from the University of Alaska Fairbanks Martin Truffer for including this work in the scope of the Malaspina surveys. We thank Brandon Tober, Stefano Nerozzi, Michael Christoffersen, Victor Devaux-Chupin and Natalie Wagner for their assistance in the field data acquisition. We also thank Brady Flinchum of Clemson University for advice and modification of his pyGiMLI scripts.

Open Research

The SEG-Y shot record data for the Sourdough glacier acquisition is archived under seismic network code 2E_2021 at the IRIS PASSCAL DMC and can be requested using dataset report number 22-003 (Holt, 2021). SEG-Y data for the Malaspina glacier acquisition is archived under seismic network code 3J_2021 at the IRIS PASSCAL DMC and can be requested using dataset report number 22-007 (Truffer et al, 2021). The GIS data collected for each site, GPR data in segy format, parameter files for the SPECFEM2D modeling, and example scripts for the refraction tomography, MASW and reflection image plotting are available at (Kuehn, 2023) https://doi.org/10.25422/azu.data.19758499.

Appendix A

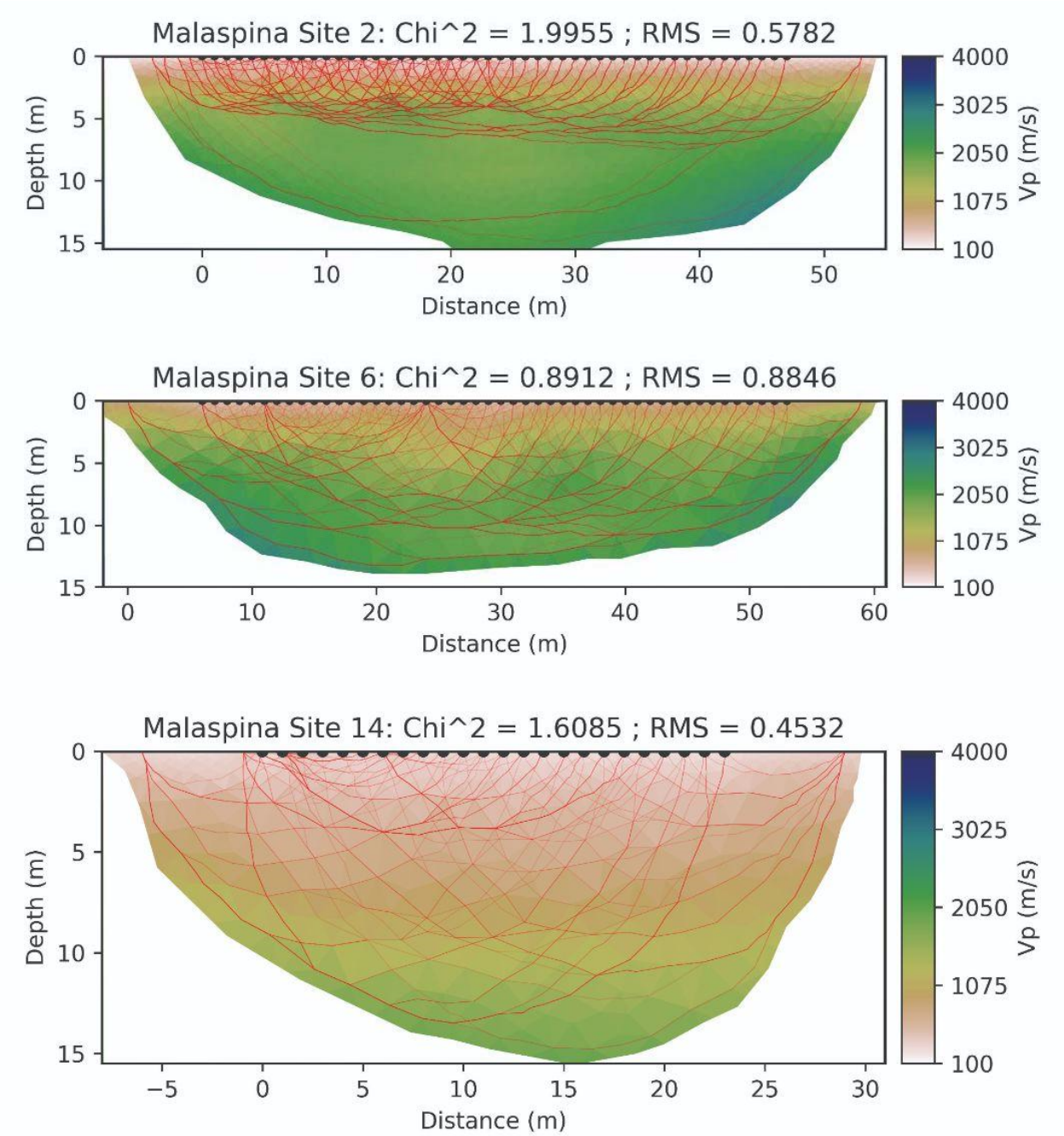
Malaspina Site 2: Chi^2 = 1.9955 ; RMS = 0.5782
Depth (m)
Distance (m)
Vp (m/s)
Malaspina Site 6: Chi^2 = 0.8912 ; RMS = 0.8846
Depth (m)
Distance (m)
Vp (m/s)
Malaspina Site 14: Chi^2 = 1.6085 ; RMS = 0.4532
Depth (m)
Distance (m)
Vp (m/s)

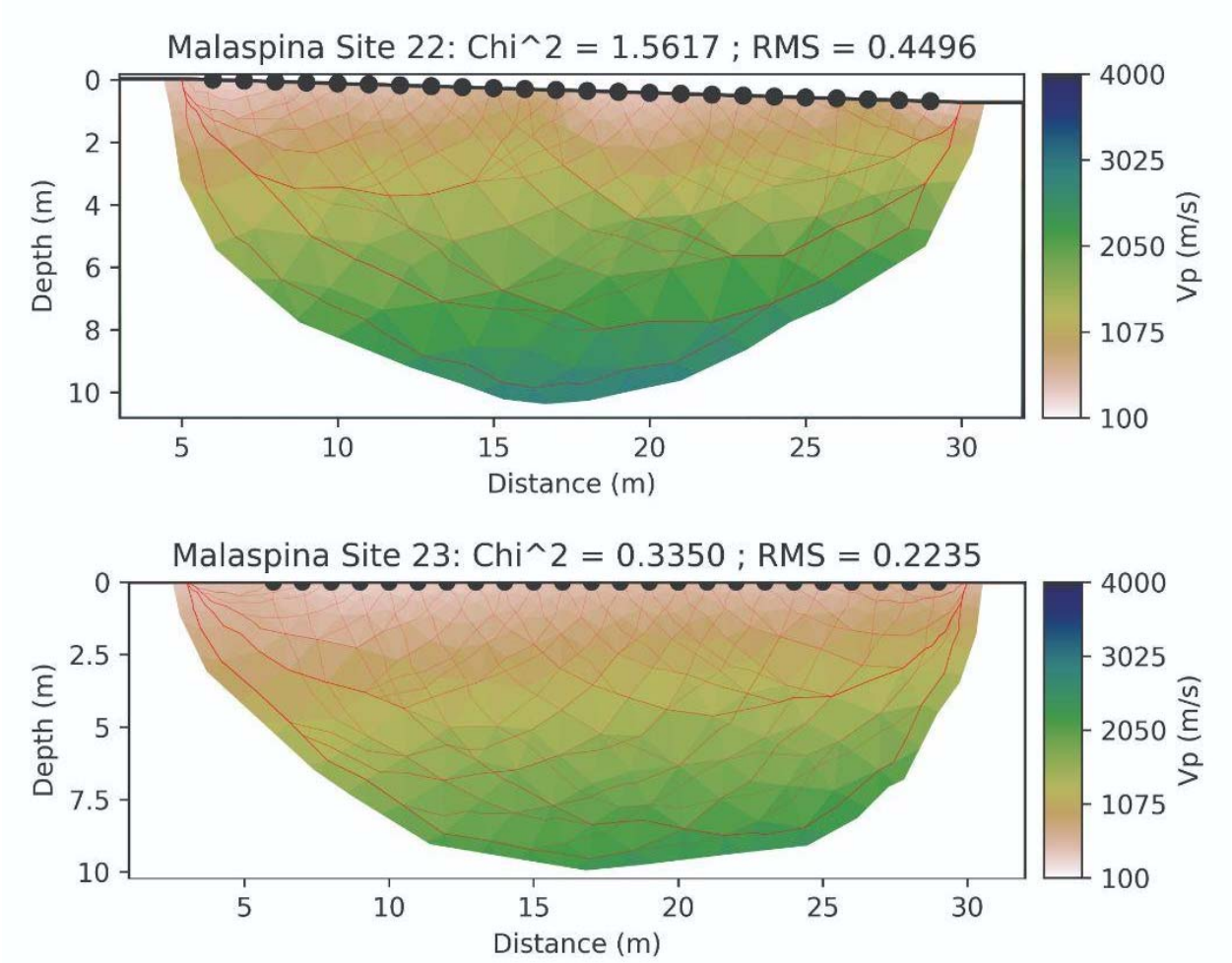
Malaspina Site 22: Chi^2 = 1.5617 ; RMS = 0.4496
Depth (m)
Distance (m)
Vp (m/s)
Malaspina Site 23: Chi^2 = 0.3350 ; RMS = 0.2235
Depth (m)
Distance (m)
Vp (m/s)

619

620

References

Abbud-Madrid, angel, Beaty, D., Boucher, D., Bussey, B., Davis, R., Gertsch, L., Hays, L., Kleinhenz, J., Meyer, M., Moats, M., Mueller, R., Paz, A., Suzuki, N., van Susante, P., Whetsel, C., & Zbinden, E. (2016, April 22). *Mars Water In-Situ Resource Utilization (ISRU) Planning (M-WIP) Study*. https://www.researchgate.net/publication/301614744_Mars_Water_In-Situ_Resource_Utilization_ISRU_Planning_M-WIP_Study

Allen, C. R., & Smith, G. I. (1953). Seismic and gravity investigations on the Malaspina Glacier, Alaska. *Transactions, American Geophysical Union*, *34*(5), 755. https://doi.org/10.1029/TR034i005p00755

Baker, G. S., Strasser, J. C., Evenson, E. B., Lawson, D. E., Pyke, K., & Bigl, R. A. (2003). Near-surface seismic reflection profiling of the Matanuska Glacier, Alaska. *GEOPHYSICS*, *68*(1), 147–156. https://doi.org/10.1190/1.1543202

Bhardwaj, A., Joshi, P. K., Snehmani, Singh, M. K., Sam, L., & Gupta, R. D. (2014). Mapping debris-covered glaciers and identifying factors affecting the accuracy. *Cold Regions Science and Technology*, *106–107*, 161–174. https://doi.org/10.1016/j.coldregions.2014.07.006

Brabham, P. J., Thomas, J., & McDonald, R. J. (2005). The terrestrial shallow seismic reflection technique applied to the characterization and assessment of shallow sedimentary environments. *Quarterly Journal of Engineering Geology and Hydrogeology*, *38*(1), 23–38. https://doi.org/10.1144/1470-9236/04-033

Bucki, A., Echelmeyer, K., & MacInnes, S. (2004). The thickness and internal structure of Fireweed rock glacier, Alaska, U.S.A., as determined by geophysical methods. *Journal of Glaciology, 50*(168), 67-75. doi:10.3189/172756504781830196

Campbell, M. J., & Ulrichs, J. (1969). Electrical properties of rocks and their significance for

lunar radar observations. *Journal of Geophysical Research*, *74*(25), 5867–5881. https://doi.org/10.1029/JB074i025p05867

Croce, F. A., & Milana, J. P. (2002). Internal structure and behaviour of a rock glacier in the Arid Andes of Argentina. *Permafrost and Periglacial Processes*, *13*(4), 289–299. https://doi.org/10.1002/ppp.431

de Pasquale, G., Valois, R., Schaffer, N., and MacDonell, S.: Contrasting geophysical signatures of a relict and an intact Andean rock glacier. The Cryosphere, 16, 1579–1596, https://doi.org/10.5194/tc-16-1579-2022, 2022.

Dix, C. H. (1955). Seismic velocities from surface measurements. *GEOPHYSICS*, *20*(1), 68–86. https://doi.org/10.1190/1.1438126

Flinchum, B. A., Holbrook, W. S., & Carr, B. J. (2022). What Do P-Wave Velocities Tell Us About the Critical Zone? *Frontiers in Water*, *3*. https://www.frontiersin.org/article/10.3389/frwa.2021.772185

Florentine, C., Skidmore, M., Speece, M., Link, C., & Shaw, C. A. (2014). Geophysical analysis of transverse ridges and internal structure at Lone Peak Rock Glacier, Big Sky, Montana, USA. *Journal of Glaciology*, *60*(221), 453–462. https://doi.org/10.3189/2014JoG13J160

Foti, S., Hollender, F., Garofalo, F., Albarello, D., Asten, M., Bard, P.-Y., Comina, C., Cornou, C., Cox, B., Di Giulio, G., Forbriger, T., Hayashi, K., Lunedei, E., Martin, A., Mercerat, D., Ohrnberger, M., Poggi, V., Renalier, F., Sicilia, D., & Socco, V. (2018). Guidelines for the good practice of surface wave analysis: A product of the InterPACIFIC project. *Bulletin of Earthquake Engineering*, *16*(6), 2367–2420. https://doi.org/10.1007/s10518-017-0206-7

Gustavson, T. C., & Boothroyd, J. C. (1987). A depositional model for outwash, sediment sources, and hydrologic characteristics, Malaspina Glacier, Alaska: A modern analog of the southeastern margin of the Laurentide Ice Sheet. *GSA Bulletin*, *99*(2), 187–200.

https://doi.org/10.1130/0016-7606(1987)99<187:ADMFOS>2.0.CO;2

Head, J. W., Marchant, D. R., Dickson, J. L., Kress, A. M., & Baker, D. M. (2010). Northern mid-latitude glaciation in the Late Amazonian period of Mars: Criteria for the recognition of debris-covered glacier and valley glacier landsystem deposits. *Earth and Planetary Science Letters*, *294*(3), 306–320. https://doi.org/10.1016/j.epsl.2009.06.041

Heincke, B., Günther, T., Dalsegg, E., Rønning, J. S., Ganerød, G. V., & Elvebakk, H. (2010). Combined three-dimensional electric and seismic tomography study on the Åknes rockslide in western Norway. *Journal of Applied Geophysics*, *70*(4), 292–306. https://doi.org/10.1016/j.jappgeo.2009.12.004

Holt, J. W., Safaeinili, A., Plaut, J. J., Head, J. W., Phillips, R. J., Seu, R., Kempf, S. D., Choudhary, P., Young, D. A., Putzig, N. E., Biccari, D., & Gim, Y. (2008). Radar Sounding Evidence for Buried Glaciers in the Southern Mid-Latitudes of Mars. *Science*, *322*(5905), 1235–1238. https://doi.org/10.1126/science.1164246

Holt, J.W. (2021). Reflection and Refraction Active Seismic Acquisition on Sourdough Rock Glacier, McCarthy, Alaska [Data set]. International Federation of Digital Seismograph Networks. https://doi.org/10.7914/SN/2E_2021

Karslı, H., & Bayrak, Y. (2004). Using the Wiener–Levinson algorithm to suppress ground-roll. *Journal of Applied Geophysics*, *55*(3–4), 187–197. https://doi.org/10.1016/j.jappgeo.2003.11.003

Killingbeck, S. F., Livermore, P. W., Booth, A. D., & West, L. J. (2018). Multimodal layered transdimensional inversion of seismic dispersion curves with depth constraints. *Geochemistry, Geophysics, Geosystems*, 19, 4957–4971. https://doi.org/10.1029/2018GC008000

Kingsley, S. A. (1986). Distributed Fiber-Optic Sensors: An Overview. *Fiber Optic and Laser Sensors III*, *0566*, 28–36. https://doi.org/10.1117/12.949760

Komatitsch, D. (1997). *Méthodes spectrales et éléments spectraux pour l'équation de*

l'élastodynamique 2D et 3D en milieu hétérogène. Institut de Physique du Globe de Paris.

Komatitsch, D., Tromp, Jeroen, & Vilotte, Jean-Pierre. (1998). The spectral element method for elastic wave equations: Application to 2D and 3D. *Bulletin of the Seismological Society of America*, *88*, 368–392.

Kuehn, T. (2023). Active Seismic Refraction, Reflection and Surface-Wave Exploration in Debris-Covered Glacial Environments, Sourdough and Malaspina Glaciers, Alaska [Dataset]. University of Arizona Research Data Repository. https://doi.org/10.25422/azu.data.19758499.v1

Langston, G., Bentley, L. R., Hayashi, M., McClymont, A., & Pidlisecky, A. (2011). Internal structure and hydrological functions of an alpine proglacial moraine. *Hydrological Processes*, *25*(19), 2967–2982. https://doi.org/10.1002/hyp.8144

Levy, J. S., Fassett, C. I., Head, J. W., Schwartz, C., & Watters, J. L. (2014). Sequestered glacial ice contribution to the global Martian water budget: Geometric constraints on the volume of remnant, midlatitude debris-covered glaciers. *Journal of Geophysical Research: Planets*, *119*(10), 2188–2196. https://doi.org/10.1002/2014JE004685

Maurer, H., & Hauck, C. (2007). Geophysical imaging of alpine rock glaciers. *Journal of Glaciology*, *53*(180), 110–120. https://doi.org/10.3189/172756507781833893

Meng, T., Petersen, E., & Holt, J. (2022). Rock glacier composition and structure from radio wave speed analysis with dipping reflector correction. Journal of Glaciology, 1-19. doi:10.1017/jog.2022.90

Merz, K., Maurer, H., Rabenstein, L., Buchli, T., Springman, S. M., & Zweifel, M. (2016). Multidisciplinary geophysical investigations over an alpine rock glacier. *GEOPHYSICS*, *81*(1), WA147–WA157. https://doi.org/10.1190/geo2015-0157.1

Monnier, S., & Kinnard, C. (2013). Internal structure and composition of a rock glacier in the Andes (upper Choapa valley, Chile) using borehole information and ground-penetrating

radar. *Annals of Glaciology*, *54*(64), 61–72. https://doi.org/10.3189/2013AoG64A107

Musgrave, A. W. (Ed.). (1967). *Seismic Refraction Prospecting*. Society of Exploration Geophysicists. https://doi.org/10.1190/1.9781560802679

Musil, M., Maurer, H., Green, A. G., Horstmeyer, H., Nitsche, F. O., Mühll, D. V., & Springman, S. (2002). Shallow seismic surveying of an Alpine rock glacier. *GEOPHYSICS*, *67*(6), 1701–1710. https://doi.org/10.1190/1.1527071

Nicholson, L., & Benn, D. I. (2006). Calculating ice melt beneath a debris layer using meteorological data. *Journal of Glaciology*, *52*(178), 463–470. https://doi.org/10.3189/172756506781828584

Olafsdottir, E. A., Erlingsson, S., & Bessason, B. (2018). Tool for analysis of multichannel analysis of surface waves (MASW) field data and evaluation of shear wave velocity profiles of soils. *Canadian Geotechnical Journal*, *55*(2), 217–233. https://doi.org/10.1139/cgj-2016-0302

Östrem, G. (1959). Ice Melting under a Thin Layer of Moraine, and the Existence of Ice Cores in Moraine Ridges. *Geografiska Annaler*, *41*(4), 228–230.

Park, C. B., Miller, R. D., & Miura, H. (2002). *Optimum Field Parameters of an MASW Survey*. 6.

Park, C. B., Miller, R. D., & Xia, J. (1999). Multichannel analysis of surface waves. *GEOPHYSICS*, *64*(3), 800–808. https://doi.org/10.1190/1.1444590

Park, C. B., Miller, R. D., Xia, J., & Ivanov, J. (2007). Multichannel analysis of surface waves (MASW)—Active and passive methods. *The Leading Edge*, *26*(1), 60–64. https://doi.org/10.1190/1.2431832Paul, F., Huggel, C., & Kääb, A. (2004). Combining satellite multispectral image data and a digital elevation model for mapping debris-covered glaciers. *Remote Sensing of Environment*, *89*(4), 510–518. https://doi.org/10.1016/j.rse.2003.11.007

Pavoni, M., Boaga, J., Wagner, F.M., Bast, A., Phillips, M. (2023).Characterization of rock glaciers environments combining structurally-coupled and petrophysically-coupled joint

751 inversions of electrical resistivity and seismic refraction datasets. Journal of Applied
752 Geophysics, 215. https://doi.org/10.1016/j.jappgeo.2023.105097.
753 Petersen, E. I., Holt, J. W., Stuurman, C. M., Levy, J. S., Nerozzi, S., Paine, J. G., Larsen, C. F.,
754 & Fahnestock, M. (2016). Sourdough Rock Glacier, Alaska: An Analog to Martian
755 Debris-Covered Glaciers. *47th Lunar and Planetary Science Conference*, 2.
756 Petersen, E. I., Levy, J. S., Holt, J. W., & Stuurman, C. M. (2020). New insights into ice
757 accumulation at Galena Creek Rock Glacier from radar imaging of its internal structure.
758 *Journal of Glaciology*, *66*(255), 1–10. https://doi.org/10.1017/jog.2019.67
759 Potter, N., Jr. (1972). Ice-Cored Rock Glacier, Galena Creek, Northern Absaroka Mountains,
760 Wyoming. *GSA Bulletin*, *83*(10), 3025–3058. https://doi.org/10.1130/0016-
761 7606(1972)83[3025:IRGGCN]2.0.CO;2
762 Press, F. (1966). SECTION 9: SEISMIC VELOCITIES. In *Geological Society of America*
763 *Memoirs* (Vol. 97, pp. 195–218). Geological Society of America.
764 https://doi.org/10.1130/MEM97-p195
765 Richart, F.E., Hall, J.R., & Woods, R.D. (1970). *Vibrations of soils and foundations*. Prentice-
766 Hall, Inc.
767 Ronczka, M., Hellman, K., Günther, T., Wisén, R., & Dahlin, T. (2017). Electric resistivity and
768 seismic refraction tomography: A challenging joint underwater survey at Äspö Hard Rock
769 Laboratory. *Solid Earth*, *8*(3), 671–682. https://doi.org/10.5194/se-8-671-2017
770 Rowan, A. V., Egholm, D. L., Quincey, D. J., & Glasser, N. F. (2015). Modelling the feedbacks
771 between mass balance, ice flow and debris transport to predict the response to climate
772 change of debris-covered glaciers in the Himalaya. *Earth and Planetary Science Letters*,
773 *430*, 427–438. https://doi.org/10.1016/j.epsl.2015.09.004
774 Rücker, C., Günther, T., & Wagner, F. M. (2017). pyGIMLi: An open-source library for modelling
775 and inversion in geophysics. *Computers & Geosciences*, *109*, 106–123.
776 https://doi.org/10.1016/j.cageo.2017.07.011

Russell, I. C. (1893). Malaspina Glacier. *The Journal of Geology*, *1*(3), 219–245.

Sauber, J., Molnia, B., Carabajal, C., Luthcke, S., & Muskett, R. (2005). Ice elevations and surface change on the Malaspina Glacier, Alaska. *Geophysical Research Letters*, *32*(23). https://doi.org/10.1029/2005GL023943

Scherler, D., Bookhagen, B., & Strecker, M. R. (2011). Spatially variable response of Himalayan glaciers to climate change affected by debris cover. *Nature Geoscience*, *4*(3), Article 3. https://doi.org/10.1038/ngeo1068

Sheriff, R. E., & Geldart, L. P. (1982). *Exploration seismology*. Cambridge University Press.

Spikes, K. T., Tisato, N., Hess, T. E., & Holt, J. W. (2019). Comparison of geophone and surface-deployed distributed acoustic sensing seismic data. *Geophysics*. https://doi.org/10.1190/geo2018-0528.1

Steeples, D. W., Green, A. G., McEvilly, T. V., Miller, R. D., Doll, W. E., & Rector, J. W. (1997). A workshop examination of shallow seismic reflection surveying. *The Leading Edge*, *16*(11), 1641–1647. https://doi.org/10.1190/1.1437543

Steeples, D. W., & Miller, R. D. (1998). Avoiding pitfalls in shallow seismic reflection surveys. *GEOPHYSICS*, *63*(4), 1213–1224. https://doi.org/10.1190/1.1444422

Truffer, M., Larsen, C., & Fahnestock, M. (2021). Basal conditions of Malaspina Glacier [Data set]. International Federation of Digital Seismograph Networks. https://doi.org/10.7914/SN/3J_2021

Tsoflias, G. P., Ivanov, J., Anandakrishnan, S., & Miller, R. (2008). Use of Active Source Seismic Surface Waves in Glaciology. *Symposium on the Application of Geophysics to Engineering and Environmental Problems 2008*, 1240–1243. https://doi.org/10.4133/1.2963234

Uyanık, O. (2011). The porosity of saturated shallow sediments from seismic compressional and shear wave velocities. *Journal of Applied Geophysics*, *73*(1), 16–24. https://doi.org/10.1016/j.jappgeo.2010.11.001

Wagner, F. M., Mollaret, C., Günther, T., Kemna, A., & Hauck, C. (2019). Quantitative imaging of water, ice and air in permafrost systems through petrophysical joint inversion of seismic refraction and electrical resistivity data. *Geophysical Journal International*, *219*(3), 1866–1875. https://doi.org/10.1093/gji/ggz402

Xie, Z., Komatitsch, D., Martin, R., & Matzen, R. (2014). Improved forward wave propagation and adjoint-based sensitivity kernel calculations using a numerically stable finite-element PML. *Geophysical Journal International*, *198*(3), 1714–1747. https://doi.org/10.1093/gji/ggu219

Yang, Z. (Joey), Dutta, U., Xu, G., Hazirbaba, K., & Marx, E. E. (2011). Numerical analysis of permafrost effects on the seismic site response. *Soil Dynamics and Earthquake Engineering*, *31*(3), 282–290. https://doi.org/10.1016/j.soildyn.2010.08.004

Yde, J. C., & Paasche, Ø. (2010). Reconstructing Climate Change: Not All Glaciers Suitable. *Eos, Transactions American Geophysical Union*, *91*(21), 189–190. https://doi.org/10.1029/2010EO210001

Yilmaz, Ö. (2001). *Seismic Data Analysis: Processing, Inversion, and Interpretation of Seismic Data*. Society of Exploration Geophysicists. https://doi.org/10.1190/1.9781560801580